Bioactive Materials 13 (2022) 312–323

Contents lists available at ScienceDirect

Bioactive Materials

journal homepage: www.keaipublishing.com/en/journals/bioactive-materials

A multifunctional nanotheranostic agent potentiates erlotinib to EGFR wild-type non-small cell lung cancer

Duo Wang [a,b,1], Jun Zhou [d,1], Weimin Fang [a,b,1], Cuiqing Huang [a,b], Zerong Chen [a,b], Meng Fan [a,b], Ming-Rong Zhang [c], Zeyu Xiao [a,b,***], Kuan Hu [c,d,*], Liangping Luo [a,b,**]

[a] Medical Imaging Center, The First Affiliated Hospital of Jinan University, Guangzhou, 510632, PR China
[b] The Guangzhou Key Laboratory of Molecular and Functional Imaging for Clinical Translation, Jinan University, Guangzhou, 510632, PR China
[c] Department of Advanced Nuclear Medicine Sciences, Institute of Quantum Medical Science, National Institutes for Quantum and Radiological Science and Technology, Chiba, 263-8555, Japan
[d] Center for Nanomedicine and Department of Anesthesiology, Brigham and Women's Hospital, Harvard Medical School, Boston, MA, 02115, USA

ARTICLE INFO

Keywords:
Non-small cell lung cancer
EGFR wild-Type
Superparamagnetic iron oxide
Erlotinib
Bevacizumab
Tumour vascular normalization

ABSTRACT

Epidermal growth factor receptor (EGFR) tyrosine kinase inhibitors (TKI), such as Erlotinib, have demonstrated remarkable efficacy in the treatment of non-small cell lung cancer (NSCLC) patients with mutated EGFR. However, the efficacy of EGFR-TKIs in wild-type (wt) EGFR tumours has been shown to be marginal. Methods that can sensitize Erlotinib to EGFR wild-type NSCLC remain rare. Herein, we developed a multifunctional superparamagnetic nanotheranostic agent as a novel strategy to potentiate Erlotinib to EGFR-wt NSCLCs. Our results demonstrate that the nanoparticles can co-escort Erlotinib and a vascular epithermal growth factor (VEGF) inhibitor, Bevacizumab (Bev), to EGFR-wt tumours. The nanotheranostic agent exhibits remarkable effects as an inhibitor of EGFR-wt tumour growth. Moreover, Bev normalizes the tumour embedded vessels, further promoting the therapeutic efficacy of Erlotinib. In addition, the tumour engagement of the nanoparticles and the vascular normalization could be tracked by magnetic resonance imaging (MRI). Collectively, our study, for the first time, demonstrated that elaborated nanoparticles could be employed as a robust tool to potentiate Erlotinib to EGFR-wt NSCLC, paving the way for imaging-guided nanotheranostics for refractory NSCLCs expressing EGFR wild-type genes.

1. Introduction

Lung cancer is the leading cause of cancer-related deaths worldwide, and non-small cell lung cancer (NSCLC) accounts for approximately 85% of all lung cancer cases [1]. The main treatment methods for NSCLC include surgical resection, radiofrequency ablation, radiotherapy and chemotherapy, targeted therapy, and immunotherapy [2]. However, despite progress in the treatment modalities, the prognosis in patients with NSCLC has not improved significantly. A large number of patients with NSCLC harbour mutations in the epidermal growth factor receptor (*EGFR*), and approximately 40–60% of these patients are of Asian origin [3]. In 90% of the cases, mutations in the *EGFR* mainly include exon 19 (ex19del) deletion or leucine to arginine substitution in exon 21 (Leu858Arg) [4].

Tyrosine kinase inhibitors (TKIs) targeting the EGFR, such as Erlotinib (Erl) and Gefitinib, can inhibit tumour growth by binding to the ATP-binding site in EGFR [5,6]. Recently, the EGFR-TKIs have been used as first-line treatment for NSCLC among patients harbouring the mutated and activated form of EGFR [7–9]. Although benefits have been observed in a subset of EGFR-wt NSCLC patients receiving TKI treatment, TKIs manifest much less activity in EGFR-wt NSCLCs [10–12]. Many efforts have been invested into unveiling the underlying

Peer review under responsibility of KeAi Communications Co., Ltd.
* Corresponding author.Department of Advanced Nuclear Medicine Sciences, Institute of Quantum Medical Science, National Institutes for Quantum and Radiological Science and Technology, Chiba, 263-8555, Japan
** Corresponding author. Medical Imaging Center, The First Affiliated Hospital of Jinan University, Guangzhou, 510632, PR China.
*** Corresponding author.Medical Imaging Center, The First Affiliated Hospital of Jinan University, Guangzhou, 510632, PR China.
E-mail addresses: zeyuxiao@jnu.edu.cn (Z. Xiao), kuan.hu@qst.go.jp (K. Hu), tluolp@jnu.edu.cn (L. Luo).
[1] These authors contributed equally to this work.

https://doi.org/10.1016/j.bioactmat.2021.10.046
Received 27 September 2021; Received in revised form 25 October 2021; Accepted 29 October 2021
Available online 4 November 2021

molecular mechanisms of erlotinib resistance in NSCLCs expressing EGFR wild-type genes [13–15]. However, the conclusions so far are debated, and further in-depth investigation is warranted. Concomitantly, different strategies have been investigated to overcome the innate resistance of wild-type EGFR NSCLCs to TKIs [16,17]. Some chemotherapies, such as the histone deacetylase (HDAC) inhibitor Panobinostat and the autophagy inhibitor Chloroquine, have been shown to sensitize EGFR-wt NSCLCs to Erlotinib [18–21]. Although these results are promising, there is still a need to develop other strategies dedicated to different sensitization mechanisms, which may improve the understanding of erlotinib resistance in EGFR-wt NSCLC and mine the best therapeutic regimens that could maximize the therapeutic efficacy of Erlotinib in EGFR-wt NSCLC.

Nanotheranostics that may combine diagnostic and therapeutic functions in one molecule have captured enormous attention in cancer intervention [22–26]. Nanotheranostic agents have been primarily pursued as a drug delivery platform for targeted transport of various drug molecules to mitigate the side effects and to elevate treatment efficacy [27–30]. Moreover, the components of the nanotheranostics could be customized as functionalities that can be tracked by different imaging modalities, *e.g.*, optical imaging, MRI, photoacoustic imaging, and radiological imaging (positron emission tomography and single photon emission computed tomography), conferring an imaging-guided mode for cancer therapy [31–34]. Besides the above characteristics, recent studies have discovered that some nanotheranostic agents, such as inorganic nanoparticles, can exert additional effects beyond their intrinsic functions, such as being involved in modulating the tumour microenvironment, leading to synergy with the drugs [35–37]. These advantages of nanotheranostics inspired us to question whether an erlotinib-based nanoagent could potentiate Erlotinib to EGFR-wt NSCLC. Towards this goal, we started exploring how nano-engineering affects the sensitivity of Erlotinib to EGFR-wt NSCLC. Furthermore, we aim to convey an imaging-guided theranostic mode to combat NSCLC tumours expressing wild-type EGFR genes.

Superparamagnetic iron oxide (SPIO) is a clinically useable nanoparticle with a wide range of applications [38–40]. SPIO has been used as a contrast agent for magnetic resonance imaging (MRI) as it is superparamagnetic and its biocompatibility can be improved by surface modification with oleic acid [41–44]. Moreover, by targeting the mitochondrial electron transport chain, SPIO nanoparticles have been identified as a therapeutic agent for cancer cells [45]. Considering the theragnostic inherence of SPIO nanoparticles, we envisioned that SPIO nanoparticles could be selected as a prototype for developing erlotinib-based nanotheranostics. Herein, we report the development of core-shelled, erlotinib-loaded nanoparticles, which feature a SPIO as the core and polyethylene glycol (PEG)−phospholipids (DSPE--PEG2000-COOH) as the shell (Scheme 1). We demonstrated that Erlotinib could be comfortably and stably embedded in the nanoparticles. Moreover, to confer the nanoparticles with active targeting ability, we engineered Bevacizumab, an anti-VEGF antibody, to the surface of the nanoparticles through a covalent conjugation. The active targeting ability of the nanoparticles and the vascular normalization were tracked by MRI. The therapeutic efficacy of the nanoformulated Erlotinib against EGFR-wt NSCLC and the synergy between Erlotinib and Bev were systematically profiled. Collectively, our results provide a strong rationale for exploring nanotheranostics to potentiate Erlotinib to EGFR-wt NSCLC.

2. Materials and methods

2.1. Preparation of Bev + Erl@MNPs

One-hundred (100) mg of DSPE-PEG-COOH (Tansh-Tech, China) (10 mg of Erlotinib (MCE, USA)) was added to 4 mL of chloroform and dissolved using ultrasound. Oleic Acid Coated Fe3O4 (Fe_3O_4@OA, 10 mg, FE concentration) (Nanoeast, China) was added to the above

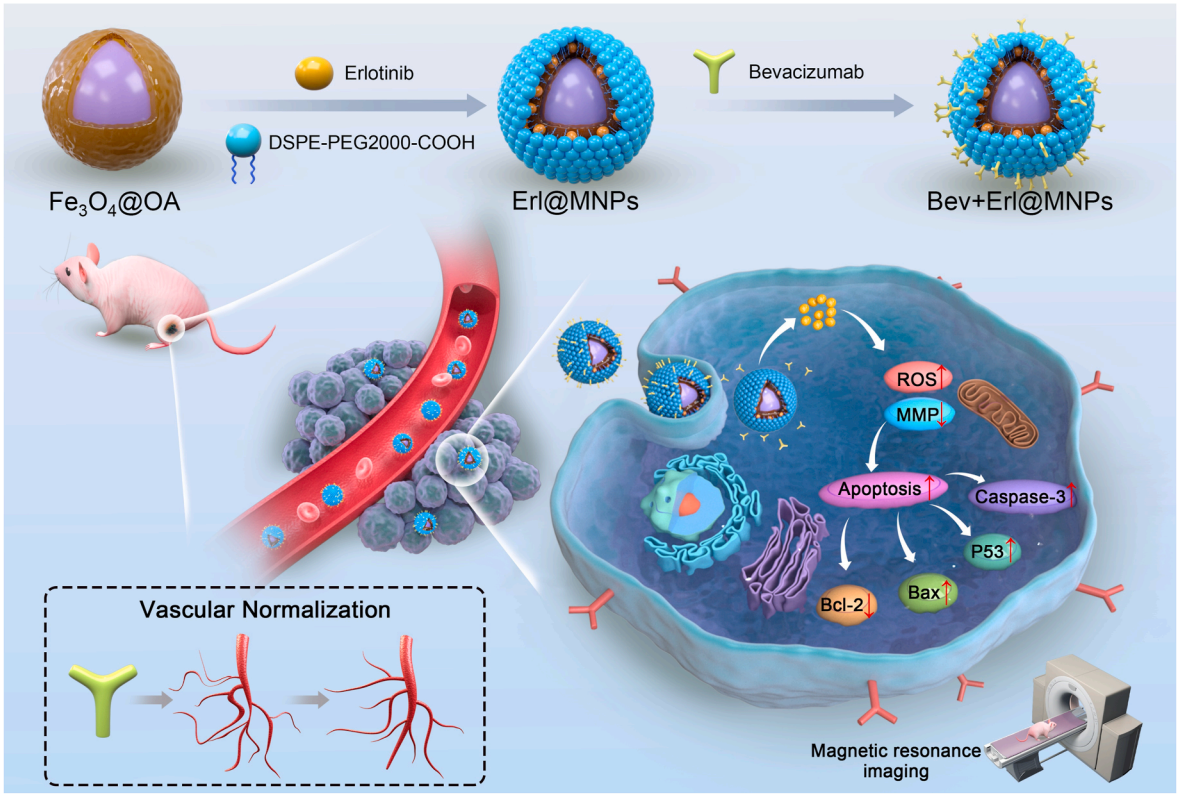

Scheme 1. Schematic diagram representing the use of Bev + Erl@MNPs to promote the normalization of tumour blood vessels and improve the diagnosis and treatment of erlotinib-resistant non-small cell lung cancer.

solution and mixed well using ultrasound. This mixture was transferred into an eggplant-shaped bottle, followed by the addition of 4 mL of deionized water. Further, this mixture was reversibly rotated at 70 °C and 20 rpm to evaporate the chloroform completely and was supplemented with pure water to prepare MNPs (Erl@MNPs).

MNPs or Erl@MNPs (10 mg, FE concentration) were weighed and dispersed in 2-(N-morpholino)ethanesulfonic acid (MES) solution (15 mM, pH 5.5) to make the final concentration 2 mg/mL. Further, 10 mg of Bev (Roche, Switzerland) (25 mg/mL) was added and adsorbed at 37 °C for 1 h. 1-Ethyl-3-(3-dimethylaminopropyl)carbodiimide (EDC) was then weighed with 15 mM MES to make a 10 mg/mL solution. Furthermore, 80 μL of EDC was added to the solution, coupled overnight at 37 °C, and purified with pure water after centrifugal ultrafiltration to prepare Bev@MNPs and Bev + Erl@MNPs. Finally, the nanoprobes were stored in water for future use.

2.2. Material characterizations

The morphology and size of the MNPs were characterized by transmission electron microscopy (TEM) (Tecnai G2 F20, FEI, USA). Zetasizer Nano ZS (Brookhaven Instruments, USA) was used to evaluate the average hydrodynamic size and surface zeta potential of the prepared MNPs. Bev coupling rate was measured by Uv–vis spectrophotometry (UV-1780, Shimadzu, Japan). The rate of release of Erl *in vitro* was determined by high-performance liquid chromatography (HPLC) (LC-15C, Shimadzu, Japan). The fluorescence spectrum of MNPs was tested using a multi-function microplate reader (Thermo Scientific, USA). The saturation magnetization of the MNPs was detected by a vibrating sample magnetometer (Quantum PPMS-9, Quantum Design Inc. USA).

2.3. Cells and animals

A549 cells were purchased from American Type Culture Collection (ATCC). Dulbecco's Modified Eagle Medium (DMEM) (Gibco, USA) was mixed with fetal bovine serum (FBS) (Hyclone, USA) and double antibiotics (streptomycin and penicillin; Hyclone, USA) according to the optimal ratio, and cultured at 37 °C in a 5% CO_2 incubator. BALB/c nude mice, weighing 14–16 g and 4–6 weeks old, were purchased from SPF Biotechnology Inc. (Beijing, China). All animal experiments were approved by the Animal Ethics Committee of Jinan University.

2.4. In vitro cell phagocytosis effect

Human NSCLC cells lines A549 were seeded in a laser confocal cell culture dish at a density of 2×10^4 cells per well. After 24 h, the cell nuclei were stained with Hoechst 33342 dye (Beyotime, China) for 30 min. The supernatant was replaced to remove the residual dye. Subsequently, 1 ml (5 μg/mL, FE concentration) Bev + Erl@MNPs was added for 30 min. The treated cells were observed under a confocal laser scanning microscope (CLSM) (LSM 800, Zeiss, Germany).

2.5. CCK8 experimental analysis

A549 cells were cultured in the logarithmic growth phase. The cell density was adjusted to 2×10^3 cells/well and was added to 96-well plates. Further, different treatment drugs—PBS (control group), MNPs, Bev@MNPs, Erl@MNPs, and Bev + Erl@MNPs—were added at 5 μg/mL (FE concentration). After 24 h, 48 h, 72 h, 96 h, and 120 h, 10 μL CCK8 colour developing solution (Beyotime, China) was added. Next, the cells were incubated at 37 °C in a 5% CO_2 incubator for 100 min. Finally, the 96-well culture plate was placed in a microplate reader to measure the absorbance of each well at 450 nm.

2.6. Cell cloning experiment

A549 cells (500 cells/well) were inoculated in a 6-well plate. PBS (control group), MNPs, Bev@MNPs, Erl@MNPs, and Bev + Erl@MNPs (5 μg/mL, FE concentration) were added to the wells. After co-cultivation for 14 days, cell colonies were formed. Then, the cells were fixed with 4% paraformaldehyde for 30 min and washed with PBS. The remaining cells were stained with crystal violet for 20 min, washed with PBS, and visible cell colonies were imaged and analysed by ImageJ.

2.7. Intracellular reactive oxygen species (ROS) detection

A 12-well plate was seeded with A549 cells (5×10^4 cells/well) for 24 h (37 °C, 5% CO_2). Subsequently, 1 ml fresh medium with PBS (control group) or MNPs, Bev@MNPs, Erl@MNPs, and Bev + Erl@MNPs (5 μg/mL, FE concentration) was added and cultured at 37 °C for 12 h. Then, the cells were incubated with DCFH-DA (Beyotime, China) solution (0.2 mM) for 0.5 h, and washed three times with PBS. Green fluorescence of the cells was recorded by CLSM (excitation wavelength: 488 nm, emission wavelength: 525 nm).

2.8. Calcein-AM/PI double staining

A549 cells (1×10^5 cells/mL) were inoculated in a 6-well plate. After overnight incubation, PBS (control group), MNPs, Bev@MNPs, Erl@MNPs, and Bev + Erl@MNPs (5 μg/mL, FE concentration) were added to the cell culture medium. The calcein-AM/PI (Beyotime, China) kit was used for staining, and images were acquired using an inverted fluorescence microscope. The excitation and emission wavelengths for green and red fluorescence are 494/517 nm and 535/617 nm, respectively.

2.9. Apoptosis detection

PBS (control group), MNPs, Bev@MNPs, Erl@MNPs, and Bev + Erl@MNPs (5 μg/mL, FE concentration) were added to A549 cells and incubated overnight. Next, the cells were trypsinized and centrifuged and gently resuspended in PBS (1×10^5 cells/mL). Subsequently, the cells were stained with 5 μL Annexin V-FITC/PI (Bestbio, China) and incubated at 25 °C in the dark for 10 min. Finally, the cells were evaluated by a flow cytometer (CytoFLEX, Beckman Coulter, USA).

2.10. In vivo imaging

In vivo MRI imaging was performed using a 1.5T Signa HDxt superconducting MR system (GE Healthcare, Milwaukee, WI, USA). The mice were injected with 200 μL (10 mg Fe/kg) of Erl@MNP and Bev + Erl@MNP and scanned with blood oxygen level-dependent-MRI (BOLD-MRI) at 2, 6, 12, 24, 48, and 72 h in the treatment cycle to observe the FE maximum accumulation in the tumour. The sequence and specific parameters of BOLD-MRI were as follows: TE = 3.4, 9.3, 15.2, 21.2, 27.1, 33, 38.9, 44.8, 50.7, 56.6, 62.5, 68.5, 74.4, 80.3, 86.2, and 92.1, TR = 160 ms; FOV = 7.5 × 6.5 cm^2; NEX = 2; and matrix size = 192 × 128. The effect of Erl@MNP and Bev + Erl@MNP at different times were expressed as the relative difference in the lateral direction (ΔR2*). The quantitative analysis of MR data was performed on post-processing workstation (AW4.5, GE Healthcare) software.

2.11. Evaluation of antitumor effect in vivo

A 100 μL suspension of A549 cells (5×10^6 cells) in PBS was mixed with 100 μL of Matrigel (BD Biosciences) and injected subcutaneously into the root of the right thigh of mice. When the mice developed tumours with an average volume of approximately 50–100 mm^3, they were randomly divided into five groups (n = 4), and 200 μL of PBS, MNPs, Bev@MNPs, Erl@MNPs, or Bev + Erl@MNPs was injected into the tail vein every 7 days (Days 0, 7, 14, and 21). The solute concentration per injection was 10 mg Fe/kg based on the body weight of the mice. Further, body weight, temperature, and tumour size were

measured every 4 days, and tumour volume (V) was calculated as V = (long diameter × short diameter^2)/2. On the 28th day of treatment, the mice were sacrificed and their tumour tissues and main organs were harvested for further testing.

2.12. T2-weighted imaging (T2WI) and intra-voxel incoherent motion diffusion weighted imaging (IVIM-DWI)

A 1.5T Signa HDxt superconducting MR system (GE Healthcare, Milwaukee, WI, USA) was used to perform MR imaging of tumours at the end of the treatment cycle. The T2WI sequence was: TE = 60 ms, TR = 4500 ms, NEX = 4, matrix = 96 × 128 and FOV = 7 × 5 cm^2. IVIM-DWI used single excitation, echo planar imaging pulse sequence and chemical shift selective saturation fat suppression technology. TE, TR, NEX, matrix and FOV parameters of IVIM-DWI were consistent with T2WI. Three orthogonal directions were set to 13 b-value diffusion gradients: 0, 25, 50, 75, 100, 150, 200, 400, 600, 800, 1,000, 1200 and 1500 s/mm^2. Functool-MADC software (AW4.5, GE Health Care, USA) was used for MRI post-processing. The D value (true diffusion coefficient) reflected the pure diffusion of water molecules. The D* value (pseudo-diffusion coefficient) was used to indicate the amount of microcirculation perfusion. The f value (perfusion fraction) represented the percentage of microcirculation perfusion in the signal attenuation caused by the total diffusion effect. Three regions of interest of the tumour largest section were drawn with reference to the T2WI image and their average was taken as the final value.

2.13. Immunofluorescence staining analysis

Apoptosis of tumour cells was detected by Terminal deoxynucleotidyl transferase dUTP nick end labelling (TUNEL, Servicebio, China) staining. CD31 (Servicebio, China) immunofluorescence staining was performed to observe the tumour microvessel density. The hypoxia-inducible factor HIF-1α (Servicebio, China) immunofluorescence staining was performed to assess the degree of tumour hypoxia. The hypoxia-inducible factor HIF-1α (Servicebio, China) immunofluorescence staining was performed to assess the degree of tumour hypoxia. Fibronectin (Servicebio, China) immunofluorescence staining was performed to determine the amount of fibronectin inside the tumour. Ki-67 (Servicebio, China) immunofluorescence staining was performed to evaluate the degree of tumour proliferation *in vivo*. Smooth muscle α-actin (α-SMA, Servicebio, China) and CD31 (Servicebio, China) were stained to assess vascular maturity index(VMI%). The VMI% calculation is based on the ratio of the overlapping area of a-SMA and CD31 to the area of CD31. Finally, ImageJ software was used to quantitatively analyse the above staining.

2.14. Western blot

The total protein lysate of tumour samples was generated by homogenizing with a RIPA Lysis Buffer (Qiagen, Venlo, Netherlands) at 4 °C. After centrifugation, the supernatant of lysate was used to quantify the protein concentration by the Pierce BCA Protein Assay Kit (Thermo Fisher Scientific) and 10 μg of protein was separated on 10% SDS-PAGE (Bio-Rad, Hercules, CA) and transferred to nitrocellulose filter (NC) membrane (Bio-Rad, Hercules, CA). NC membrane was blocked with 5% bovine serum albumin (BSA) in triethanolamine buffered saline (TBS) for 1 h and then incubated with primary antibodies for MMP9, MMP2, P53, Caspase-3, Bcl-2, Bax and β-actin (1: 1000, Abcam, USA) overnight. Next, the membranes were incubated with HRP-coupled secondary antibody in a shaker for 1 h and was then visualized by chemiluminescence. Finally, the protein band intensity was quantified by ImageJ.

2.15. Biosafety assessment of MNPs in vivo

Briefly, MNPs were injected into mice via the tail vein (30 mg FE/kg) to obtain blood samples at 0, 7, 15, and 30 days. Then, alanine aminotransferase, aspartate aminotransferase, albumin, total protein, serum cystatin C, creatinine clearance test, urea, and urinalysis were assessed to evaluate liver and kidney function.

2.16. Statistics analyses

Statistical analyses were performed and graphs were generated using SPSS software (version 22.0; IBM Corporation, USA) and GraphPad Prism 8.0 (GraphPad Software Inc., San Diego, CA). The numerical results were expressed as mean ± standard deviations. Statistical significance between the groups was determined by *t*-test or one-way analysis of variance (ANOVA). Statistical significance was set at a P-value < 0.05. A * indicates $P < 0.05$, ** indicates $P < 0.01$, and *** indicates $P < 0.001$.

3. Results and discussion

3.1. Synthesis and characterization of Bev + Erl@MNPs

In this study, the reverse evaporation method [46] was used to prepare ultra-small magnetic particle micelles (Fig. 1A). TEM analysis showed that the synthesized MNPs had a magnetic core structure surrounded by a white lipid layer (Fig. 1B), suggesting that DSPE-PEG2000 was successfully modified on the surface of Fe_3O_4. Erlotinib was successfully loaded into the MNPs, as evidenced by an increase in the average hydrodynamic size from 18.2 nm (MNPs) to 24.4 nm (Erl@MNPs, Fig. 1C). As per the calibration curve (Fig. S1), the final drug loading efficiency and encapsulation rate for Erl were approximately 4.33% and 97.8%, respectively. Additionally, HPLC showed that under conditions resembling the tumour microenvironment (TME), the drug release rate was significantly increased (Fig. S2). After surface modification, the average Zeta potential of the nanoparticles changed from −43.8 mV to −16.9 mV (Fig. 1D), and the average hydrodynamic size increased to 28.3 nm correspondingly (Fig. 1C). This indicated successful modification of Bev (0.85 mg/mg FE) to the surface of the MNPs. There was no significant change in the average hydrodynamic size of the Bev + Erl@MNPs after 7 days of incubation in PBS and mouse serum, indicating that Bev + Erl@MNPs had good water solubility and stability (Fig. 1E). The saturation magnetization of the Bev + Erl@MNPs was 42 emu/g. The hysteresis curve validated that the Bev + Erl@MNPs exhibited good superparamagnetism (Figs. 1F and S3). The concentration of nanoparticles positively correlated with the MR relaxation signal, indicating that the nanoparticles had good T2WI performance (Fig. 1F). Notably, Bev + Erl@MNPs induced negligible haemolysis at concentrations below 200 μg/mL (Fig. 1G).

3.2. In vitro toxicity of Bev + Erl@MNPs

A549 cells, an EGFR-wt NSCLC-derived cell line known to be resistant to Erlotinib, were used to evaluate cell phagocytosis and the *in vitro* toxicity of Bev + Erl@MNP [16]. To enable the optical tracking of Bev + Erl@MNP, we used an indocyanine green (ICG) dye to label Bev + Erl@MNP. The fluorescence spectrum showed that the characteristic infrared absorption peak of Bev + Erl@MNPs@ICG appeared at approximately 820 nm (Fig. S4), indicating that ICG was successfully labelled to the nanoparticles. Fluorescent imaging showed that Bev + Erl@MNPs@ICG has good phagocytosis in A549 cells (Fig. 2A). Next, we evaluated the cell effects of the nanoparticles. MNPs exhibited good safety at concentrations below 10 μg/mL, whereas obvious cell death was observed at higher concentrations (25 and 50 μg/mL) (Fig. 2B). The IC_{50} of Erl@MNPs in A549 cells was significantly lower than that of Erlotinib. These results indicate that nanoengineering can enhance the

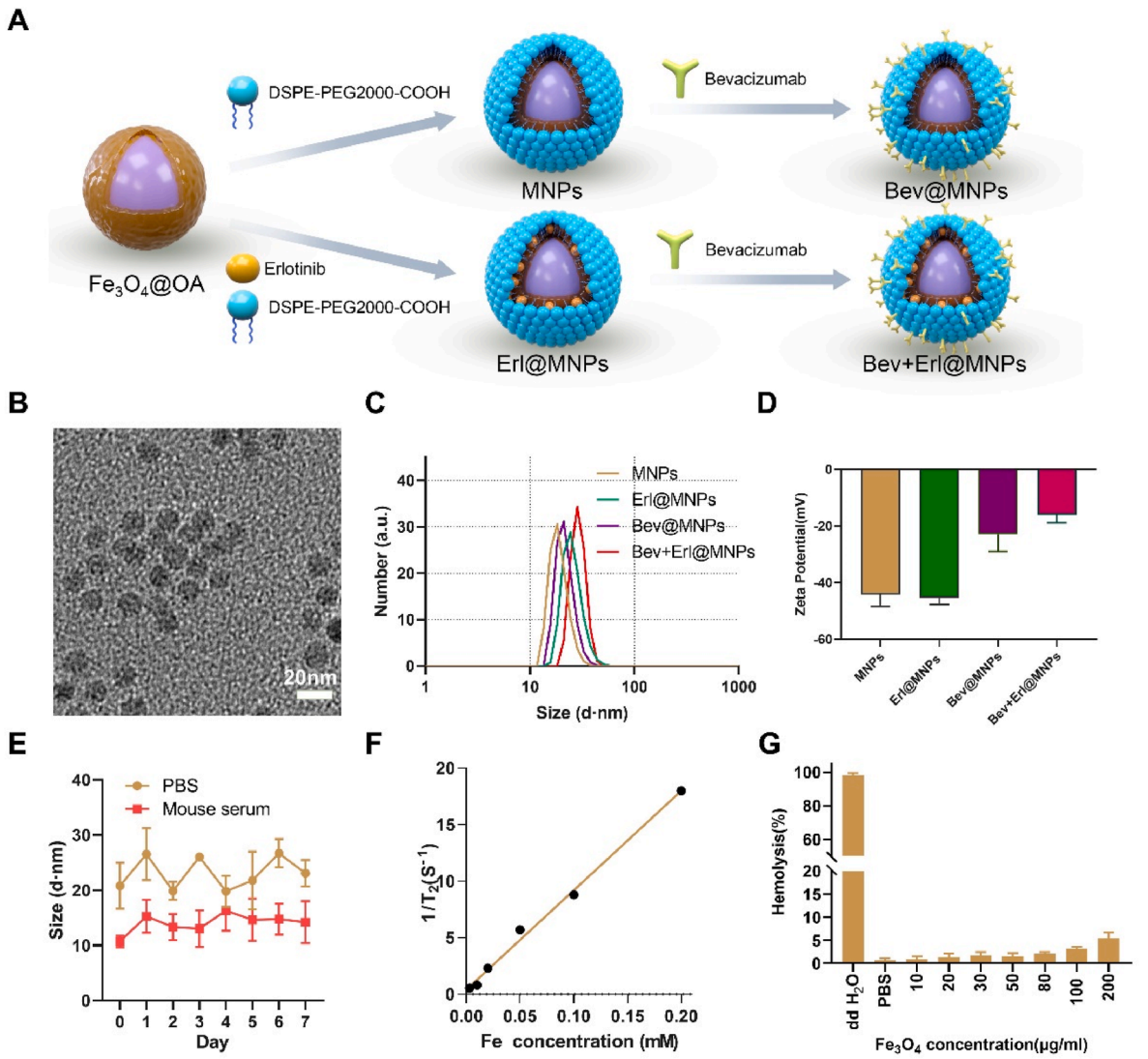

Fig. 1. Preparation and characterization of Bev + Erl@MNPs. (A) Bev + Erl@MNPs were prepared by the reverse evaporation method. (B) Transmission electron microscope (TEM) image of MNPs. (C) Size distribution of MNPs, Erl@MNPs, Bev@MNPs and Bev + Erl@MNPs. (D) Zeta potentials of MNPs, Erl@MNPs, Bev@MNPs and Bev + Erl@MNPs. (E) The changes in hydrodynamic size of Bev + Erl@MNPs in PBS and mouse serum. (F) The *in vitro* T2-weighted MR images of different concentrations of Bev + Erl@MNPs and the corresponding relaxation rate r2. (G) The blood compatibility of Bev + Erl@MNPs was evaluated by calculating the rate of haemolysis in red blood cell suspension.

therapeutic efficacy of Erlotinib in Erlotinib-resistant A549 cells (Fig. 2C). Furthermore, a CCK8 analysis was conducted to study the cell proliferation in A549 cells treated with different groups of nanoparticles (Fig. 2D). Both Erl@MNPs and Bev + Erl@MNPs had apparent inhibitory effects on cell proliferation, and Bev + Erl@MNPs had a better effect than the other treatment groups. Finally, the results of a cloning experiment confirmed the cell-killing effects of Bev + Erl@MNPs (Fig. 2E–F).

3.3. Cell apoptosis analysis

Intracellular reactive oxygen species (ROS) were analysed. Both Erl@MNPs and Bev + Erl@MNPs elicited the generation of massive intracellular ROS, whereas MNP and Bev@MNP treatment caused no observable changes in the ROS levels in A549 cells (Fig. 3A–B). We next performed Calcein-AM/PI double staining (Fig. 3C–D) and flow cytometric analysis to detect the apoptosis rate of cells (Fig. 3E–F). The apoptosis rate of cells treated with Bev + Erl@MNPs was the highest among the five groups. Moreover, the Bev + Erl@MNP treatment resulted in a higher cell apoptosis rate than the Erl@MNPs group (40.27% vs. 31.62%, respectively). Notably, the apoptosis rate of cells treated with Bev@MNPs differs significantly from that of the control group (Fig. 3F). Overall, these results indicate that Erlotinib-loaded MNPs can exhibit a good apoptosis-inducing effect and Bev can enhance the *in vitro* therapeutic effect of Erlotinib. Considering the co-regulatory relationship between the EGFR and VEGF pathways, dual inhibition of VEGF and EGFR pathways is a promising strategy to enhance cell apoptosis of NSCLC cells *in vivo* [47,48].

3.4. MRI imaging and in vivo antitumor study

To profile the tumour targetability of the nanoparticles, we performed MRI in A549 xenograft mice, which were intravenously administered with Bev + Erl@MNPs or Erl@MNPs. MRI was performed at different time points post-injection (p.i.). From 2 h to 72 h p.i., we observed significant differences in the cellular magnetic signals (ΔR2*) between the two groups, and the maximal difference appeared at 12 h p.i. (Fig. 4A–B). These results indicate that Bev modification elevated the tumour uptake of the nanoparticles, which could lead to a higher Erlotinib concentration in the TME.

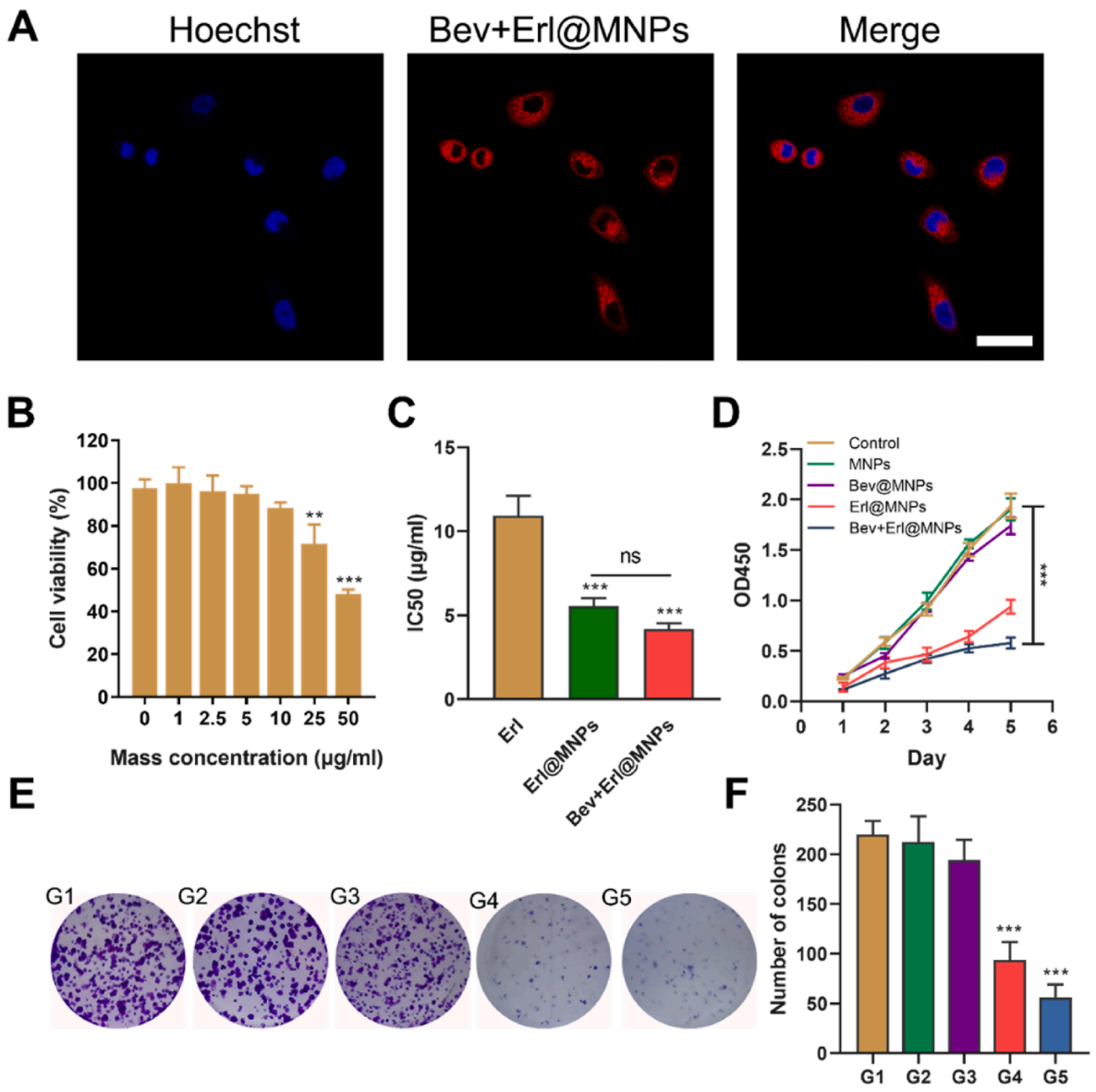

Fig. 2. Analyses of phagocytosis and cytotoxicity of cells treated with magnetic nanoparticles (MNPs). (A) *In vitro* phagocytosis of Bev + Erl@MNPs in A549 cells, scale bar = 20 μm. (B) Cell viability of A549 cells treated with different concentrations of MNPs. (C) IC_{50} values of Erlotinib, Erl@MNPs, and Bev + Erl@MNPs. (D) CCK8 analysis of A549 cells at different days after treating with PBS, MNPs, Bev@MNPs, Erl@MNPs or Bev + Erl@MNPs. (E) Cell cloning analysis in A549 cells treated with PBS (G1), MNPs (G2), Bev@MNPs (G3), Erl@MNPs (G4) or Bev + Erl@MNPs (G5). (F) Statistical analysis of colon numbers of different from Fig. E. Data are expressed as mean ± SD (n = 3), and all statistical analysis was performed by *t*-test or one-way ANOVA.

Based on the excellent *in vitro* antitumor effect and remarkable tumour uptake of Bev + Erl@MNPs, we next conducted an *in vivo* antitumor experiment. A549 tumour-bearing xenograft mice were randomly divided into five groups and were separately administered PBS, MNPs, Bev@MNPs, Erl@MNPs, or Bev + Erl@MNPs according to the treating schedule illustrated in Fig. 4C. As shown in Fig. 4D, MNPs showed no inhibition of tumour growth. In comparison, the Bev@MNPs, Erl@MNPs, and Bev + Erl@MNPs groups all showed significant tumour inhibition effects, with an order of Bev + Erl@MNPs > Erl@MNPs > Bev@MNPs. Tumour weight at the end of the therapy further confirmed that Bev + Erl@MNPs achieved the best therapeutic effects (Fig. 4E). Notably, a significant difference in tumour weight exists between the Bev + Erl@MNPs and Erl@MNPs groups, indicating that Bev modification synergizes with Erlotinib to inhibit tumour growth *in vivo*. The body weight and temperature of mice were monitored during the treating process (Figs. 4F and S5). No pronounced difference was observed among the groups, suggesting no acute toxicity induced by the nanoparticles.

Functional MRI was performed to profile the vessel conditions after treatment. Representative mice from five groups at the end of the therapy (day 28) were subjected to MRI. Major indicators reflecting the tumour size and vessel normalization, including T2WI, D, D*, and f, were analysed (Fig. 4G). First, T2WI slices perfectly annotated the tumour size, in good agreement with the *ex vivo* tumour weight data. Additionally, the pseudo-colour image of D showed the highest red signals in the Bev + Erl@MNP treated group, indicating the highest degree of diffusion of water molecules (Fig. 4D and H). Similarly, the D* and f showed the highest values in the Bev + Erl@MNP groups, indicating the best tumour blood perfusion (Fig. 4G and H–I). Collectively, these results suggest that the Bev + Erl@MNPs showed the best effects to induce vascular normalization during the antitumor treatment [49,50].

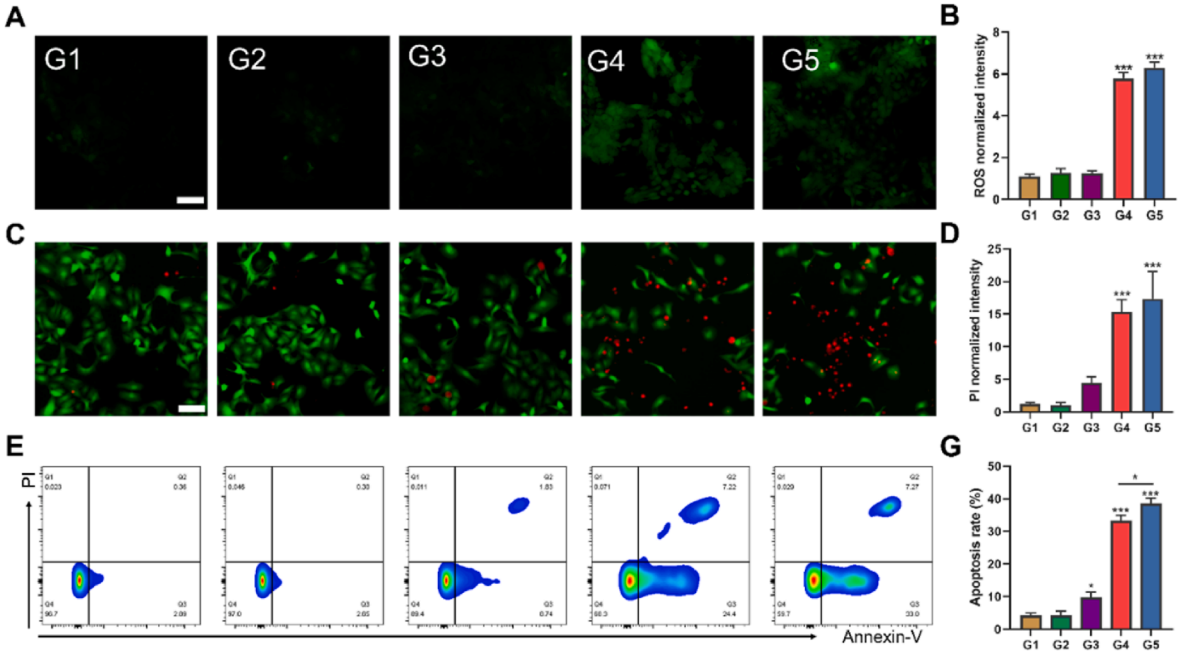

Fig. 3. Intracellular ROS and cell apoptosis analysis. (A) Apoptosis analyses in A549 cells treated with PBS (G1), MNPs (G2), Bev@MNPs (G3), Erl@MNPs (G4) or Bev + Erl@MNPs (G5), scale bar = 50 μm. (B) Normalized intracellular ROS intensity in A549 cells from Fig. 3A. (C) Calcein-AM/propidium iodide (PI) double staining of A549 cells treated with PBS (G1), MNPs (G2), Bev@MNPs (G3), Erl@MNPs (G4) or Bev + Erl@MNPs (G5), scale bar = 50 μm. (D) Normalized PI intensity in A549 cells from Fig. 3C. (E) Flow cytometrical analysis of apoptosis of A549 cells treated with PBS (G1), MNPs (G2), Bev@MNPs (G3), Erl@MNPs (G4) or Bev + Erl@MNPs (G5). (F) Apoptosis rate of A549 cells from Fig. 3E. Data are expressed as mean ± SD (n = 3), and all statistics are analysed by one-way ANOVA.

3.5. Histological analysis and Western blot

Histological analysis was performed on mice tumour tissues to verify the therapeutic effect of Bev + Erl@MNPs. Ki67 staining showed that MNP treated tumours have a similar cell proliferation index as PBS treated tumours. In contrast, the three groups treated with MNP-based nanoparticles showed decreased Ki67 staining intensity. Specifically, the Ki67 positive area in Bev + Erl@MNP treated tumours was significantly lower than that in Erl@MNP treated tumours (Fig. 5A–B). This trend was further verified by terminal deoxynucleotidyl transferase dUTP nick end labelling (TUNEL) staining, which suggested significantly increased cell apoptosis in the Bev + Erl@MNP treated tumours compared with that in other groups (Fig. 5A and C). Fibronectin is a lateral evaluation index of tumour stability [51,52]. Fibronectin staining in the tumour tissues showed significantly increased fibronectin production in the Bev + Erl@MNP group compared with that in other groups (Fig. 5A and D), confirming the effectivity of the nanoagent in reducing the migration of tumour cells. Additionally, CD31 staining indicated a significant reduction in the microvessel density in the Bev@MNP and Bev + Erl@MNP groups compared with that in other groups (Fig. 5A and E), suggesting the ability of Bev to inhibit tumour angiogenesis [48,53,54]. The reduction in tumour microvessels is usually accompanied by hypoxia inside the tumour. However, in our study, the HIF-1α intensity, an index reflecting the degree of hypoxia, was reduced in both the Bev@MNP and Bev + Erl@MNP groups (Fig. 5A and F), indicating the improvement of the hypoxia conditions induced by Bev-modified nanoparticles. This phenomenon is consistent with previous reports that low-dose of Bev can inhibit tumour angiogenesis and suppress the hypoxic TME. Collectively, these results indicate that the administration of multiple small doses of Bev + Erl@MNPs may lead to normalization of tumour blood vessels, improve the hypoxic TME, and achieve a balance between vascular suppression and hypoxia improvement during treatment.

In addition, we performed a Western blot assay to probe the expression of apoptosis-related proteins. Matrix metalloproteinase 2 (MMP2) and MMP9, responsible for cancer cell migration and metastasis, are essential indicators reflecting the invasiveness of the tumours. The MNP treatment showed remarkable effects to down-regulate MMP2 and MMP9 in tumour cells (Fig. 5G–H). Among the five groups, Bev + Erl@MNP-treated tumours expressed the least MMP2 and MMP9 proteins. Moreover, the analysis showed that the highest level of proapoptotic protein Bax was expressed in Bev + Erl@MNP treated tumours, consistent with the lowest Bcl-2 protein expression (Fig. 5G and I). Consistent with these results, the tumour suppressor P53 and an apoptosis executioner, caspase-3, showed the highest expression in the Bev + Erl@MNP treated tumours (Fig. 5G and I).

3.6. Tumour vessel normalization

To dissect the details regarding the vessel normalization dynamics after drug administration, we sampled the tumours at 0, 1, 3, 5, and 7 days post-injection of Bev + Erl@MNPs (PBS) and stained them for CD31 and α-SMA (Figs. 6A and S6). Fig. 6B–C showed that the formation of perivascular cells increased on the third day after administering Bev + Erl@MNPs. Interestingly, this phenomenon was further strengthened on day 5 and weakened on day 7. These results clearly indicate the normalization of tumour blood vessels induced by the nanoagents. The process of blood vessel normalization also brings about the improvement of hypoxic microenvironment(Fig. S7). Moreover, it suggested that the normalization effects are dynamically changed. In the future, a study that investigates the correlation between drug administration frequency and therapeutic effects is worthy as an effective strategy to maximize the therapeutic potentials of Bev + Erl@MNPs. Collectively, the above results further confirm that Bev + Erl@MNPs can assist in the normalization of tumour blood vessels, achieve antitumor angiogenesis, prevent the side effects of tumour hypoxia, and delay resistance to Erl.

3.7. Biosafety study

First, we treated the mouse liver parenchymal cells (AML-12) and mouse fibroblast cells (L929) with MNPs. Even at a high concentration (100 μg/ml), the nanoagents caused negligible cell death (Fig. S8).

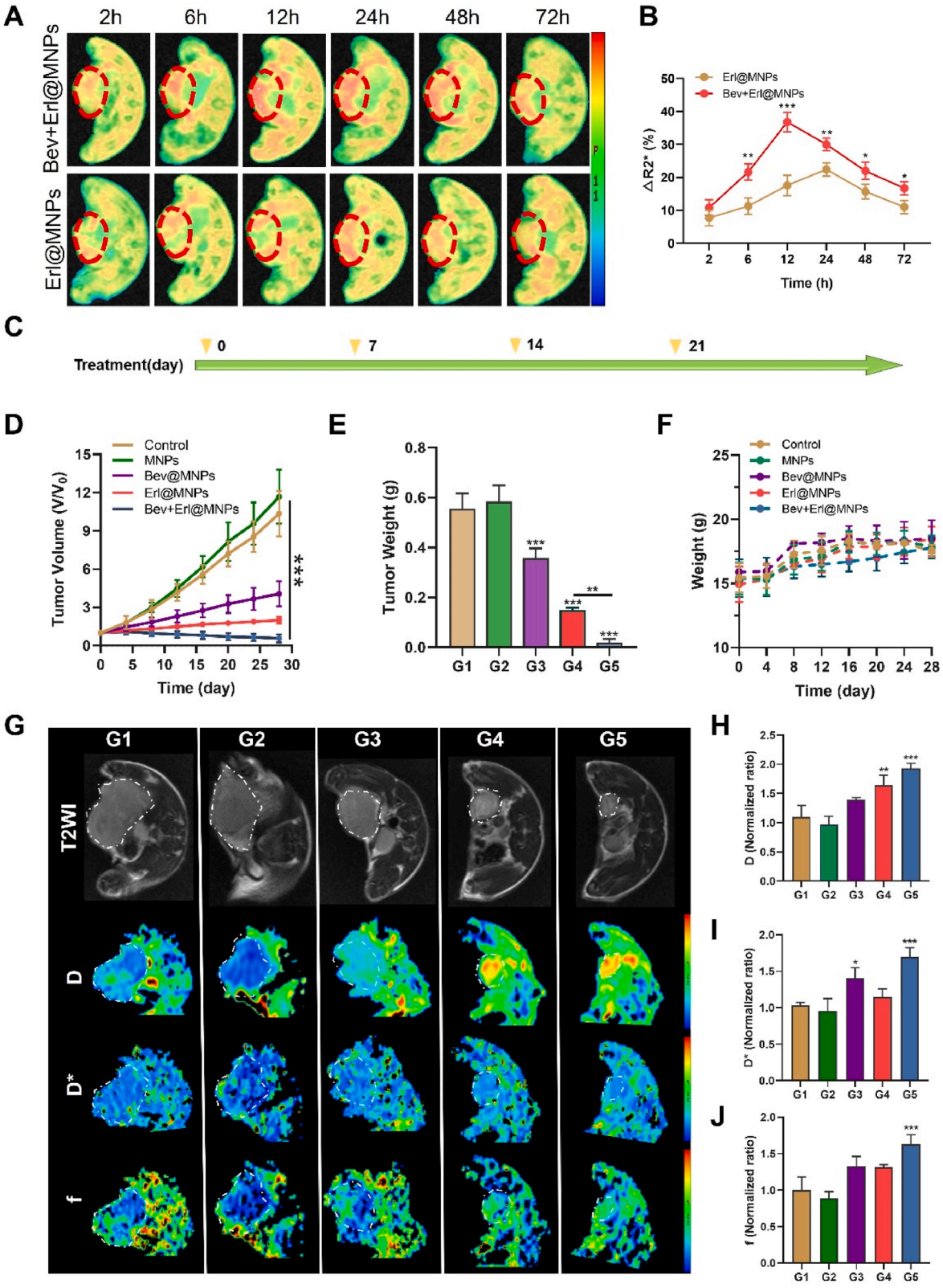

Fig. 4. MRI and analysis of anti-tumour effects of magnetic nanoparticles (MNPs). (A) MRI tracking of the tumour accumulation of Erl@MNPs and Bev + Erl@MNPs. (B) Magnetic signal changes in tumours against time. (C) Schematic illustration of the treatment plan in A549 zenograft. (D) Tumour growth curves in mice treated with PBS (G1), MNPs (G2), Bev@MNPs (G3), Erl@MNPs (G4) or Bev + Erl@MNPs (G5). (E) Tumour weight at the end of therapy. (F) Body weight of mice. (G) *In vivo* T2WI imaging and D, D*, and f pseudo-colour images acquired in mice treated with PBS (G1), MNPs (G2), Bev@MNPs (G3), Erl@MNPs (G4) or Bev + Erl@MNPs (G5). (H) Normalized ratio of D, D*, and f. Data are expressed as mean ± SD (n = 4), and all statistics are analysed by *t*-test or one-way ANOVA.

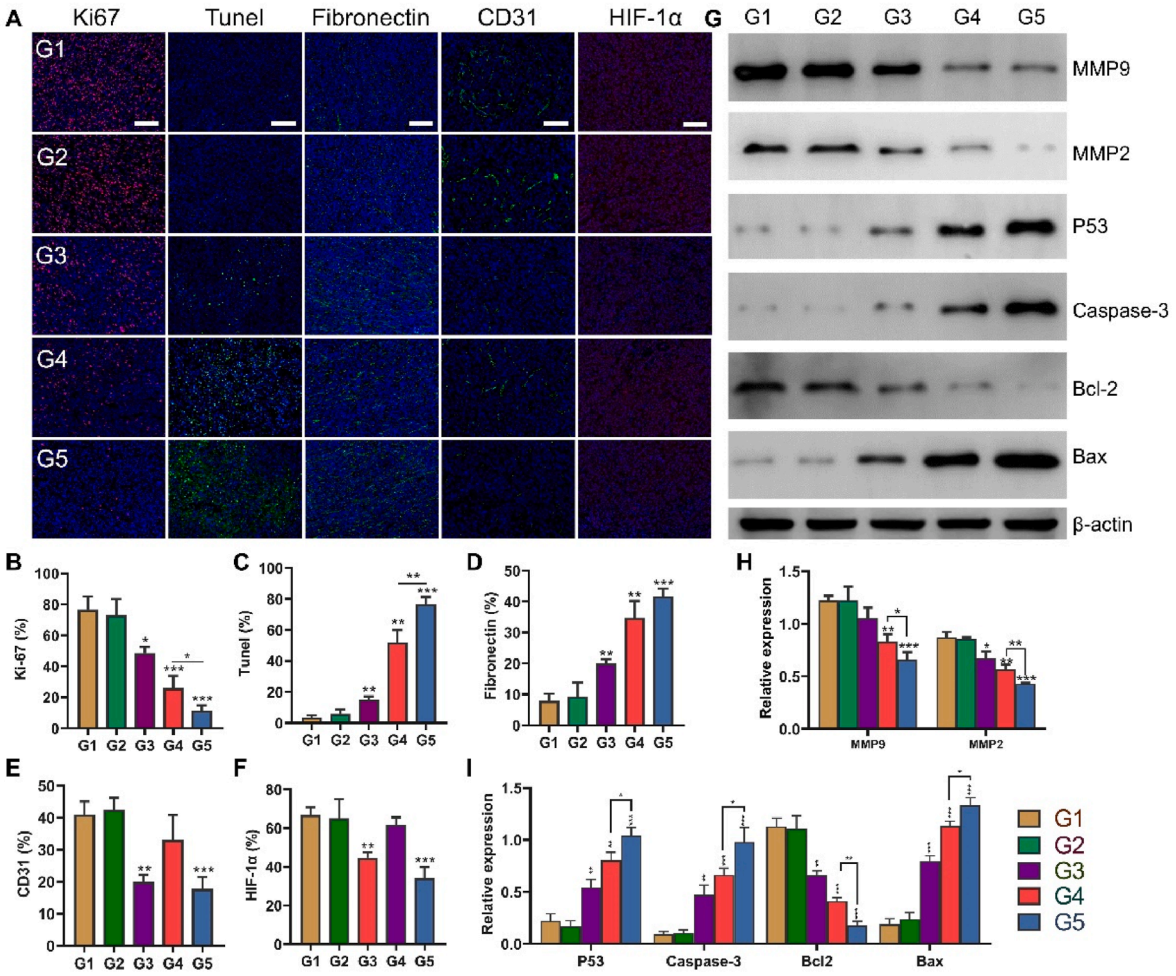

Fig. 5. Immunofluorescence analyses of tumour tissues from mice treated with different nanoagents. (A) Ki67, TUNEL, fibronectin, CD31, and HIF-1α stained images of tumour tissues from mice treated with PBS (G1), MNPs (G2), Bev@MNPs (G3), Erl@MNPs (G4) or Bev + Erl@MNPs (G5), scale bar = 100 μm. (B) Ki67 (C) TUNEL (D) Fibronectin (E) CD31 and (F) HIF-1a signals in the tumour was quantified according to the data in panel A. (G) Western analysis of MMP-9, MMP2, P53, Capsase-3, Bcl-2, and Bax expression levels in tumours from mice treated with Bev + Erl@MNPs. (H) Relative expression of MMP9 and MMP2 (I) P53, Caspase-3, Bcl-2, and Bax was quantified according to the data in panel H. Data are expressed as mean ± SD (n = 3), and all statistics are analysed by one-way ANOVA.

Moreover, we performed blood biochemical and histological analyses of major organs of healthy mice intravenously injected with MNPs. The blood biochemical analysis showed no significant variations before and after drug administration (Fig. S9). H&E staining of the heart, liver, spleen, lung, and kidney of the mice at the end of the treatment showed no obvious abnormalities and lesions (Fig. S10). At the same time, the different groups did not show organ toxicity and blood routine changes in a short period of time after administration (Fig. S11). These results suggest that the nanoagent has good *in vivo* safety and does not cause serious side effects in the major organs.

4. Conclusion

TKIs, such as Erlotinib, have garnered great success in the treatment of NSCLC harbouring mutated EGFR genes. However, their efficacy in EGFR-wt NSCLC remains moderate. Moreover, methods that can sensitize EGFR-wt NSCLC to Erlotinib are rare, partially due to the reason that the underlying molecular mechanism leading to erlotinib resistance in NSCLC expressing wild-type EGFR is unclear. Despite this, some combinatorial chemotherapies have been reported to be capable of overcoming the innate erlotinib resistance. However, none of these strategies have been validated in clinical trials. Nowadays, there is still an unmet need for other combinatorial strategies that can potentiate Erlotinib to EGFR-wt NSCLC, that can particularly address the different sensitization mechanisms. In this study, we demonstrated that an erlotinib-based nanotheranostic agent successfully reverses the resistance of EGFR-wt NSCLC to Erlotinib. Furthermore, our results indicated that anti-VEGF, in combination with Erlotinib, could be a potential combinatorial regimen to enhance the therapeutic effects of Erlotinib. In addition, the superparamagnetic inherence of the SPIO enables *in vivo* tracking to assess the target engagement of the nanotheranostic agent and vascular normalization after therapy. Overall, these results, for the first time, indicate that an elaborated nanoagent could be used to potentiate Erlotinib to EFGR-wt NSCLC. Given that several chemodrug-based nanoagents have been approved for use in the clinic, we can expect the clinical translation of this erlotinib-based nanotheranostic agent in the future to combat NSCLC among patients expressing wild-type EGFR genes.

Conflict of interest

The authors declare no conflict of interest.

CRediT authorship contribution statement

L.L., K.H.and Z.X. conceived and planned the experiments. J.Z., K.H. and M.Z. conducted the synthesis and characterization of the nanomaterials. D.W., W.F., Z.C., M.F and C.H. performed the experiments and

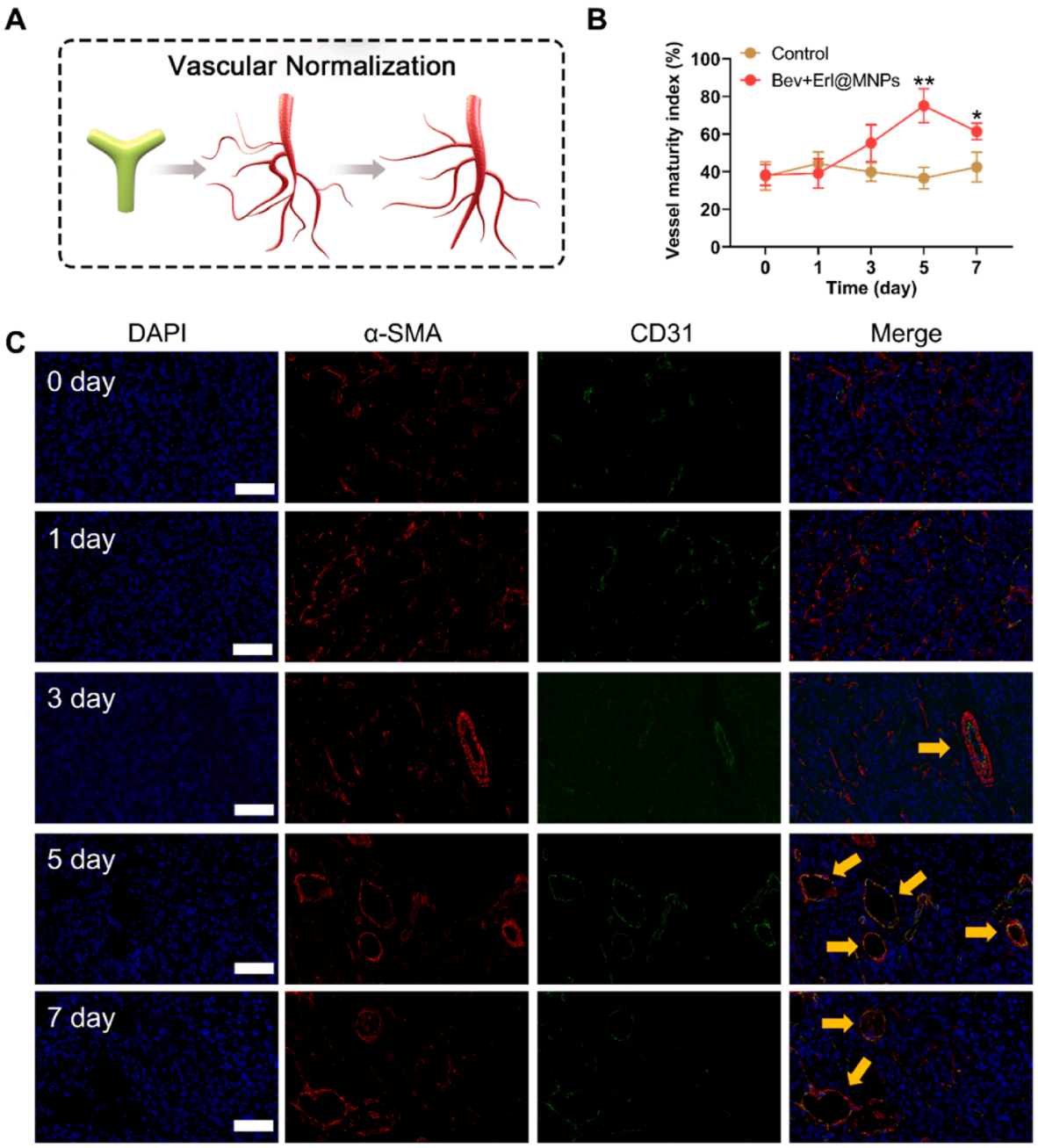

Fig. 6. Vascularization in tumour tissues of mice after treatment with Bev + Erl@MNPs. (A) Schematic diagram of bevacizumab-induced vascular normalization. (B) Vascular maturity index in tumour tissues from mice treated with PBS and Bev + Erl@MNPs. (C) CD31 and α-SMA staining in tumour tissues from mice treated with Bev + Erl@MNPs, scale bar = 100 μm.Data are expressed as mean ± SD (n = 3), and all statistics are analysed by *t*-test.

analysed data for the vitro and vivo study. K.H., D.W. and C.H.. wrote the manuscript, which was reviewed and edited by all co-authors.

Acknowledgments

This study was supported partly by grants from the Natural Science Foundation of China (81771973, 81971672 and 82102005), Key Program of the Natural Science Foundation of Guangdong Province (2018B0303110011), Guangzhou Key Laboratory of Molecular and Functional Imaging for Clinical Translation (201905010003), Fundamental Research Funds for the Central Universities (21620308 and 21620101), JSPS KAKENHI grant Nos. 21H02873, 21K07659, and 20H03635, and the AMED Moonshot Research and Development Program (Grant No 21zf0127003h001).

Appendix A. Supplementary data

Supplementary data to this article can be found online at https://doi.org/10.1016/j.bioactmat.2021.10.046.

References

[1] F. Bray, J. Ferlay, I. Soerjomataram, R.L. Siegel, L.A. Torre, A. Jemal, Global cancer statistics 2018: GLOBOCAN estimates of incidence and mortality worldwide for 36 cancers in 185 countries, Ca - Cancer J. Clin. 68 (2018) 394–424.
[2] R.S. Herbst, D. Morgensztern, C. Boshoff, The biology and management of non-small cell lung cancer, Nature 553 (2018) 446–454.
[3] K.D. Miller, L. Nogueira, A.B. Mariotto, J.H. Rowland, K.R. Yabroff, C.M. Alfano, A. Jemal, J.L. Kramer, R.L. Siegel, Cancer treatment and survivorship statistics, Ca - Cancer J. Clin. 69 (2019) 363–385, 2019.
[4] J.G. Paez, P.A. Janne, J.C. Lee, S. Tracy, H. Greulich, S. Gabriel, P. Herman, F. J. Kaye, N. Lindeman, T.J. Boggon, K. Naoki, H. Sasaki, Y. Fujii, M.J. Eck, W.

R. Sellers, B.E. Johnson, M. Meyerson, EGFR mutations in lung cancer: correlation with clinical response to gefitinib therapy, Science 304 (2004) 1497–1500.
[5] C.J. Langer, Epidermal growth factor receptor inhibition in mutation-positive non-small-cell lung cancer: is afatinib better or simply newer? J. Clin. Oncol. 31 (2013) 3303–3306.
[6] R. Rosell, E. Carcereny, R. Gervais, A. Vergnenegre, B. Massuti, E. Felip, R. Palmero, R. Garcia-Gomez, C. Pallares, J.M. Sanchez, R. Porta, M. Cobo, P. Garrido, F. Longo, T. Moran, A. Insa, F. De Marinis, R. Corre, I. Bover, A. Illiano, E. Dansin, J. de Castro, M. Milella, N. Reguart, G. Altavilla, U. Jimenez, M. Provencio, M.A. Moreno, J. Terrasa, J. Muñoz-Langa, J. Valdivia, D. Isla, M. Domine, O. Molinier, J. Mazieres, N. Baize, R. Garcia-Campelo, G. Robinet, D. Rodriguez-Abreu, G. Lopez-Vivanco, V. Gebbia, L. Ferrera-Delgado, P. Bombaron, R. Bernabe, A. Bearz, A. Artal, E. Cortesi, C. Rolfo, M. Sanchez-Ronco, A. Drozdowskyj, C. Queralt, I. de Aguirre, J.L. Ramirez, J.J. Sanchez, M. A. Molina, M. Taron, L. Paz-Ares, Erlotinib versus standard chemotherapy as first-line treatment for European patients with advanced EGFR mutation-positive non-small-cell lung cancer (EURTAC): a multicentre, open-label, randomised phase 3 trial, Lancet Oncol. 13 (2012) 239–246.
[7] A. Passaro, T. Mok, S. Peters, S. Popat, M.J. Ahn, F. de Marinis, Recent advances on the role of EGFR tyrosine kinase inhibitors in the management of NSCLC with uncommon, non exon 20 insertions, EGFR mutations, J. Thorac. Oncol. 16 (2021) 764–773.
[8] W.H. Hsu, J.C. Yang, T.S. Mok, H.H. Loong, Overview of current systemic management of EGFR-mutant NSCLC, Ann. Oncol. 29 (2018) i3–i9.
[9] T.S. Mok, Y.L. Wu, S. Thongprasert, C.H. Yang, D.T. Chu, N. Saijo, P. Sunpaweravong, B. Han, B. Margono, Y. Ichinose, Y. Nishiwaki, Y. Ohe, J. J. Yang, B. Chewaskulyong, H. Jiang, E.L. Duffield, C.L. Watkins, A.A. Armour, M. Fukuoka, Gefitinib or carboplatin-paclitaxel in pulmonary adenocarcinoma, N. Engl. J. Med. 361 (2009) 947–957.
[10] G. Metro, R. Chiari, S. Duranti, A. Siggillino, M.J. Fischer, D. Giannarelli, V. Ludovini, C. Bennati, L. Marcomigni, A. Baldi, M. Giansanti, V. Minotti, L. Crino, Impact of specific mutant KRAS on clinical outcome of EGFR-TKI-treated advanced non-small cell lung cancer patients with an EGFR wild type genotype, Lung Cancer 78 (2012) 81–86.
[11] Q. Xu, F. Zhou, H. Liu, T. Jiang, X. Li, Y. Xu, C. Zhou, Consolidative local ablative therapy improves the survival of patients with synchronous oligometastatic NSCLC harboring EGFR activating mutation treated with first-line EGFR-TKIs, J. Thorac. Oncol. 13 (2018) 1383–1392.
[12] J. Mazieres, F. Barlesi, I. Rouquette, O. Molinier, B. Besse, I. Monnet, C. Audigier-Valette, A.C. Toffart, P.A. Renault, S. Fraboulet, S. Hiret, B. Mennecier, D. Debieuvre, V. Westeel, P. Masson, A. Madroszyk-Flandin, E. Pichon, A.B. Cortot, E. Amour, F. Morin, G. Zalcman, D. Moro-Sibilot, P.J. Souquet, Randomized phase II trial evaluating treatment with EGFR-TKI associated with antiestrogen in women with nonsquamous advanced-stage NSCLC: IFCT-1003 LADIE trial, Clin. Cancer Res. 26 (2020) 3172–3181.
[13] S. Nukaga, H. Yasuda, K. Tsuchihara, J. Hamamoto, K. Masuzawa, I. Kawada, K. Naoki, S. Matsumoto, S. Mimaki, S. Ikemura, K. Goto, T. Betsuyaku, K. Soejima, Amplification of EGFR wild-type Alleles in non-small cell lung cancer cells confers acquired resistance to mutation-selective EGFR tyrosine kinase inhibitors, Cancer Res. 77 (2017) 2078–2089.
[14] P. Pronzato, M. Loprevite, A. Brianti, C. Defferrari, G. Catania, F. Grossi, Disease stabilization (SD) as a surrogate end-point in advanced non-small cell lung cancer (NSCLC) patients treated with erlotinib (E) or gefitinib (G), J. Clin. Oncol. 25 (2007) 18115, 18115.
[15] R. Thomas, S. Srivastava, R.R. Katreddy, J. Sobieski, Z. Weihua, Kinase-inactivated EGFR is required for the survival of wild-type EGFR-expressing cancer cells treated with tyrosine kinase inhibitors, Int. J. Mol. Sci. 20 (2019).
[16] K. Suda, H. Mizuuchi, K. Sato, T. Takemoto, T. Iwasaki, T. Mitsudomi, The insulin-like growth factor 1 receptor causes acquired resistance to erlotinib in lung cancer cells with the wild-type epidermal growth factor receptor, Int. J. Cancer 135 (2014) 1002–1006.
[17] J. Raimbourg, M.P. Joalland, M. Cabart, L. de Plater, F. Bouquet, A. Savina, D. Decaudin, J. Bennouna, F.M. Vallette, L. Lalier, Sensitization of EGFR wild-type non-small cell lung cancer cells to EGFR-tyrosine kinase inhibitor erlotinib, Mol. Cancer Therapeut. 16 (2017) 1634–1644.
[18] K. Yonesaka, K. Zejnullahu, N. Lindeman, A.J. Homes, D.M. Jackman, F. Zhao, A. M. Rogers, B.E. Johnson, P.A. Janne, Autocrine production of amphiregulin predicts sensitivity to both gefitinib and cetuximab in EGFR wild-type cancers, Clin. Cancer Res. 14 (2008) 6963–6973.
[19] Y. Zou, Y.H. Ling, J. Sironi, E.L. Schwartz, R. Perez-Soler, B. Piperdi, The autophagy inhibitor chloroquine overcomes the innate resistance of wild-type EGFR non-small-cell lung cancer cells to erlotinib, J. Thorac. Oncol. 8 (2013) 693–702.
[20] G. Greve, I. Schiffmann, D. Pfeifer, M. Pantic, J. Schuler, M. Lubbert, The pan-HDAC inhibitor panobinostat acts as a sensitizer for erlotinib activity in EGFR-mutated and -wildtype non-small cell lung cancer cells, BMC Cancer 15 (2015) 947.
[21] T. Li, Y.H. Ling, R. Perez-Soler, Tumor dependence on the EGFR signaling pathway expressed by the p-EGFR:p-AKT ratio predicts erlotinib sensitivity in human non-small cell lung cancer (NSCLC) cells expressing wild-type EGFR gene, J. Thorac. Oncol. 3 (2008) 643–647.
[22] K. Hu, L. Xie, Y. Zhang, M. Hanyu, Z. Yang, K. Nagatsu, H. Suzuki, J. Ouyang, X. Ji, J. Wei, H. Xu, O.C. Farokhzad, S.H. Liang, L. Wang, W. Tao, M.R. Zhang, Marriage of black phosphorus and Cu(2+) as effective photothermal agents for PET-guided combination cancer therapy, Nat. Commun. 11 (2020) 2778.
[23] S. Mura, P. Couvreur, Nanotheranostics for personalized medicine, Adv. Drug Deliv. Rev. 64 (2012) 1394–1416.
[24] H. Chen, W. Zhang, G. Zhu, J. Xie, X. Chen, Rethinking cancer nanotheranostics, Nat Rev Mater 2 (2017).
[25] W. Chen, C. Liu, X. Ji, J. Joseph, Z. Tang, J. Ouyang, Y. Xiao, N. Kong, N. Joshi, O. C. Farokhzad, W. Tao, T. Xie, Stanene-based nanosheets for β-elemene delivery and ultrasound-mediated combination cancer therapy, Angew Chem. Int. Ed. Engl. 60 (2021) 7155–7164.
[26] X. Ji, L. Ge, C. Liu, Z. Tang, Y. Xiao, W. Chen, Z. Lei, W. Gao, S. Blake, D. De, B. Shi, X. Zeng, N. Kong, X. Zhang, W. Tao, Capturing functional two-dimensional nanosheets from sandwich-structure vermiculite for cancer theranostics, Nat. Commun. 12 (2021) 1124.
[27] Y. Liu, J. Wang, Q. Xiong, D. Hornburg, W. Tao, O.C. Farokhzad, Nano-bio interactions in cancer: from therapeutics delivery to early detection, Acc. Chem. Res. 54 (2021) 291–301.
[28] T. Lammers, F. Kiessling, W.E. Hennink, G. Storm, Nanotheranostics and image-guided drug delivery: current concepts and future directions, Mol. Pharm. 7 (2010) 1899–1912.
[29] W. Chen, C.A. Cheng, J.I. Zink, Spatial, temporal, and dose control of drug delivery using noninvasive magnetic stimulation, ACS Nano 13 (2019) 1292–1308.
[30] W. Chen, C.A. Glackin, M.A. Horwitz, J.I. Zink, Nanomachines and other caps on mesoporous silica nanoparticles for drug delivery, Acc. Chem. Res. 52 (2019) 1531–1542.
[31] F.M. Kievit, M. Zhang, Cancer nanotheranostics: improving imaging and therapy by targeted delivery across biological barriers, Adv. Mater. 23 (2011) H217–H247.
[32] S. Kunjachan, J. Ehling, G. Storm, F. Kiessling, T. Lammers, Noninvasive imaging of nanomedicines and nanotheranostics: principles, progress, and prospects, Chem. Rev. 115 (2015) 10907–10937.
[33] Y. Liu, P. Bhattarai, Z. Dai, X. Chen, Photothermal therapy and photoacoustic imaging via nanotheranostics in fighting cancer, Chem. Soc. Rev. 48 (2019) 2053–2108.
[34] J. Ouyang, L. Wang, W. Chen, K. Zeng, Y. Han, Y. Xu, Q. Xu, L. Deng, Y.N. Liu, Biomimetic nanothylakoids for efficient imaging-guided photodynamic therapy for cancer, Chem. Commun. 54 (2018) 3468–3471.
[35] W. Tao, N. Kong, X. Ji, Y. Zhang, A. Sharma, J. Ouyang, B. Qi, J. Wang, N. Xie, C. Kang, H. Zhang, O.C. Farokhzad, J.S. Kim, Emerging two-dimensional monoelemental materials (Xenes) for biomedical applications, Chem. Soc. Rev. 48 (2019) 2891–2912.
[36] L.S. Lin, J. Song, L. Song, K. Ke, Y. Liu, Z. Zhou, Z. Shen, J. Li, Z. Yang, W. Tang, G. Niu, H.H. Yang, X. Chen, Simultaneous fenton-like ion delivery and glutathione depletion by MnO2 -based nanoagent to enhance chemodynamic therapy, Angew Chem. Int. Ed. Engl. 57 (2018) 4902–4906.
[37] J. Ouyang, L. Zhang, L. Li, W. Chen, Z. Tang, X. Ji, C. Feng, N. Tao, N. Kong, T. Chen, Y.N. Liu, W. Tao, Cryogenic exfoliation of 2D stanene nanosheets for cancer theranostics, Nano-Micro Lett. 13 (2021) 90.
[38] Y. Liu, W. Zhen, L. Jin, S. Zhang, G. Sun, T. Zhang, X. Xu, S. Song, Y. Wang, J. Liu, H. Zhang, All-in-One theranostic nanoagent with enhanced reactive oxygen species generation and modulating tumor microenvironment ability for effective tumor eradication, ACS Nano 12 (2018) 4886–4893.
[39] A.P. Khandhar, P. Keselman, S.J. Kemp, R.M. Ferguson, P.W. Goodwill, S. M. Conolly, K.M. Krishnan, Evaluation of PEG-coated iron oxide nanoparticles as blood pool tracers for preclinical magnetic particle imaging, Nanoscale 9 (2017) 1299–1306.
[40] A.H. Lu, E.L. Salabas, F. Schuth, Magnetic nanoparticles: synthesis, protection, functionalization, and application, Angew Chem. Int. Ed. Engl. 46 (2007) 1222–1244.
[41] N. Fernandez-Bertolez, C. Costa, F. Brandao, J.A. Duarte, J.P. Teixeira, E. Pasaro, V. Valdiglesias, B. Laffon, Evaluation of cytotoxicity and genotoxicity induced by oleic acid-coated iron oxide nanoparticles in human astrocytes, Environ. Mol. Mutagen. 60 (2019) 816–829.
[42] H. Wei, O.T. Bruns, M.G. Kaul, E.C. Hansen, M. Barch, A. Wisniowska, O. Chen, Y. Chen, N. Li, S. Okada, J.M. Cordero, M. Heine, C.T. Farrar, D.M. Montana, G. Adam, H. Ittrich, A. Jasanoff, P. Nielsen, M.G. Bawendi, Exceedingly small iron oxide nanoparticles as positive MRI contrast agents, Proc. Natl. Acad. Sci. U. S. A. 114 (2017) 2325–2330.
[43] K. Liu, S. Tan, Y. Chai, D. Chen, H. Song, C.W. Zhang, Y. Shi, J. Liu, W. Tan, J. Lyu, S. Gao, J. Yan, J. Qi, G.F. Gao, Structural basis of anti-PD-L1 monoclonal antibody avelumab for tumor therapy, Cell Res. 27 (2017) 151–153.
[44] Z. Xiao, Y. You, Y. Liu, L. He, D. Zhang, Q. Cheng, D. Wang, T. Chen, C. Shi, L. Luo, NIR-triggered blasting nanovesicles for targeted multimodal image-guided synergistic cancer photothermal and chemotherapy, ACS Appl. Mater. Interfaces 13 (2021) 35376–35388.
[45] C. He, S. Jiang, H. Jin, S. Chen, G. Lin, H. Yao, X. Wang, P. Mi, Z. Ji, Y. Lin, Z. Lin, G. Liu, Mitochondrial electron transport chain identified as a novel molecular target of SPIO nanoparticles mediated cancer-specific cytotoxicity, Biomaterials 83 (2016) 102–114.
[46] K. Otake, T. Shimomura, T. Goto, T. Imura, T. Furuya, S. Yoda, Y. Takebayashi, H. Sakai, M. Abe, Preparation of liposomes using an improved supercritical reverse phase evaporation method, Langmuir 22 (2006) 2543–2550.
[47] G.N. Naumov, M.B. Nilsson, T. Cascone, A. Briggs, O. Straume, L.A. Akslen, E. Lifshits, L.A. Byers, L. Xu, H.K. Wu, P. Janne, S. Kobayashi, B. Halmos, D. Tenen, X.M. Tang, J. Engelman, B. Yeap, J. Folkman, B.E. Johnson, J.V. Heymach, Combined vascular endothelial growth factor receptor and epidermal growth factor receptor (EGFR) blockade inhibits tumor growth in xenograft models of EGFR inhibitor resistance, Clin. Cancer Res. 15 (2009) 3484–3494.

[48] L.A. Byers, J.V. Heymach, Dual targeting of the vascular endothelial growth factor and epidermal growth factor receptor pathways: rationale and clinical applications for non-small-cell lung cancer, Clin. Lung Cancer 8 (Suppl 2) (2007) S79–S85.
[49] C. Shi, D. Liu, Z. Xiao, D. Zhang, G. Liu, G. Liu, H. Chen, L. Luo, Monitoring tumor response to antivascular therapy using non-contrast intravoxel incoherent motion diffusion-weighted MRI, Cancer Res. 77 (2017) 3491–3501.
[50] D. Le Bihan, E. Breton, D. Lallemand, P. Grenier, E. Cabanis, M. Laval-Jeantet, MR imaging of intravoxel incoherent motions: application to diffusion and perfusion in neurologic disorders, Radiology 161 (1986) 401–407.
[51] L.A. Griggs, N.T. Hassan, R.S. Malik, B.P. Griffin, B.A. Martinez, L.W. Elmore, C. A. Lemmon, Fibronectin fibrils regulate TGF-beta1-induced epithelial-mesenchymal transition, Matrix Biol. 60–61 (2017) 157–175.
[52] L.M. Knowles, L.A. Gurski, J.K. Maranchie, J. Pilch, Fibronectin matrix formation is a prerequisite for colonization of kidney tumor cells in fibrin, J. Cancer 6 (2015) 98–104.
[53] P. Bocca, E. Di Carlo, I. Caruana, L. Emionite, M. Cilli, B. De Angelis, C. Quintarelli, A. Pezzolo, L. Raffaghello, F. Morandi, F. Locatelli, V. Pistoia, I. Prigione, Bevacizumab-mediated tumor vasculature remodelling improves tumor infiltration and antitumor efficacy of GD2-CAR T cells in a human neuroblastoma preclinical model, OncoImmunology 7 (2017), e1378843.
[54] R. Rosell, U. Dafni, E. Felip, A. Curioni-Fontecedro, O. Gautschi, S. Peters, B. Massutí, R. Palmero, S.P. Aix, E. Carcereny, M. Früh, M. Pless, S. Popat, A. Kotsakis, S. Cuffe, P. Bidoli, A. Favaretto, P. Froesch, N. Reguart, J. Puente, L. Coate, F. Barlesi, D. Rauch, M. Thomas, C. Camps, J. Gómez-Codina, M. Majem, R. Porta, R. Shah, E. Hanrahan, R. Kammler, B. Ruepp, M. Rabaglio, M. Kassapian, N. Karachaliou, R. Tam, D.S. Shames, M.A. Molina-Vila, R.A. Stahel, Erlotinib and bevacizumab in patients with advanced non-small-cell lung cancer and activating EGFR mutations (BELIEF): an international, multicentre, single-arm, phase 2 trial, The Lancet Respiratory Medicine 5 (2017) 435–444.